**Revision 2**

# Multiple generations of tourmaline from Yushishanxi leucogranite in South Qilian of western China record a complex formation history from B-rich melt to hydrothermal fluid

Tao Liu [a], Shao-Yong Jiang [a,b]*

[a] *State Key Laboratory of Geological Processes and Mineral Resources, Collaborative Innovation Center for Exploration of Strategic Mineral Resources, School of Earth Resource, China University of Geosciences, Wuhan 430074, P.R. China*

[b] *Key Laboratory of Geological Survey and Evaluation of Ministry of Education, China University of Geosciences, Wuhan 430074, P.R. China*

*Corresponding author, E-mail address: Shyjiang@cug.edu.cn (S.-Y. Jiang)

## ABSTRACT

One tourmaline-bearing leucogranite dike occurs in the Yushishanxi Nb-Ta mining area in the Yushishan district of the South Qilian orogenic belt in western China. Abundant tourmalines have been identified in the leucogranite, including disseminated, crosscutting quartz-tourmaline veins and tourmaline veinlets. Detailed petrological, geochemical, and boron isotopic studies indicate that these tourmalines have distinctive core-rim zoning signatures and significant chemical variations, which can be divided into four paragenetic generations. Generation-I tourmalines in the leucogranite have a magmatic origin, and were followed by hydrothermal Generations-II, III, and IV. Tourmalines from all four generations belong to the alkali group and the schorl-dravite solid solution series. The most notable features are the variations in Mg, Fe, and Ca contents. The variable Mg/(Mg+Fe) ratios from I to IV may be attributed to the multiple influx and/or interaction of initially magma-derived hydrothermal fluid with surrounding rocks, magma-derived Fe-rich hydrothermal fluid, and external metamorphic fluid. In-situ B-isotope analyses of tourmaline yield a total range of $\delta^{11}B$ values from -11.7‰ to -6.0‰. The earliest Generation-I tourmalines have $\delta^{11}B$ values of -11.1‰ to -9.6‰, whereas Generation-II and III tourmalines record a higher $\delta^{11}B$ value of -9.5‰ to -6.0‰ and -9.3‰ to -6.9‰, respectively. Such an increase is mainly controlled by boron-isotope fractionation between melt-fluid and tourmaline-fluid, Rayleigh fractionation, and also, to some extent, by a hydrothermal recharge from the same magma source. Generation-IV

tourmalines have the lightest B-isotope values (down to -11.7‰). This shift back to lighter B-isotopes in the Generation-IV cannot be explained by closed-system crystallization and isotope fractionation of known phases. Alternatively, a lighter source of boron via fluid circulation from the surrounding metamorphic rocks can explain this light boron isotope compositions. Therefore, we propose that an isotopically light fluid may have derived from B release during mica breakdown within the surrounding metamorphic rocks.

**Keywords:** tourmaline, geochemistry, boron isotope, magmatic-hydrothermal evolution, multiple generations, South Qilian

## INTRODUCTION

Tourmaline is the most common borosilicate mineral in igneous and metamorphic rocks and ore deposits because of its wide P-T stability range and resistance to later alteration (e.g., Hawthorne and Dirlam, 2011; Marschall and Jiang, 2011; Trumbull et al., 2020). Tourmaline can crystallize as an early magmatic mineral (Bénard et al., 1985; London and Manning, 1995; London et al., 1996; London, 1999) or as a late mineral in a transitional stage from late solidus (magmatic) to early subsolidus (hydrothermal) conditions (Sinclair and Richardson, 1992; London and Manning, 1995; Buriánek and Novák, 2007; Yang et al., 2015). The tourmaline crystal structure can generally accommodate a wide variety of cations with different size and valence, typically producing a complex typology and variable compositions. Owing to its negligible intra-crystalline diffusion (von Goerne et al., 1999; van Hinsberg et al., 2011), tourmaline can preserve chemical fingerprints of the composition of the melt or fluid from which it crystallized (Trumbull and Chaussidon, 1999; Trumbull et al., 2008; Henry and Dutrow, 2012). As a result, multistage crystallization and chemical zoning in tourmalines with corresponding compositional variations can provide valuable information regarding the physic-chemical condition variations of fluid and their evolution history, as well as petrogenesis and ore genesis during the growth of tourmaline (e.g., Mlynarczyk and Williams, 2006; Duchoslav et al., 2017; Yu et al., 2017; Codeço, et al., 2017, 2019). In granite-related hydrothermal systems, the presence of tourmaline indicates the involvement of boron and other volatiles in magmatic differentiation, magmatic degassing, fluid exsolution, wall-rock

alteration, and metal transport and deposition (e.g., London et al., 1996; Smith and Yardley, 1996; Jiang et al., 1998, 2002, 2008). Boron-isotopes of tourmaline can have a wide range, and the $^{11}B/^{10}B$ ratios of different reservoirs are markedly different making them an excellent tracer for the source of boron, origin, and evolution of fluids, P-T conditions, and water/rock interactions (e.g., Palmer et al., 1992; Palmer and Swihart, 1996; Marschall et al., 2006, 2008; Trumbull et al., 2008, 2013; Yang and Jiang, 2012; Yang et al., 2015; Siegel et al., 2016; Zhao et al., 2019; Trumbull et al., 2020).

In the Yushishanxi Nb-Ta rare metal deposit, South Qilian orogenic belt of western China, tourmaline is abundant and represented by disseminations or fracture-filling veins in the leucogranite in the mining area. In this paper, we present data on major elements and boron-isotopic compositions in the tourmalines. Different types of tourmalines show systematic core-rim zonations and also chemical variations corresponding to their different generations. Considering that compositional growth-zone can significantly record evolution processes, we have used these tourmalines from Yushishanxi leucogranite to reconstruct their crystallization processes, boron mobilization, and infiltration history during magmatic-, magmatic-hydrothermal transition, and hydrothermal processes.

## GEOLOGICAL SETTING

The Qilian-Qaidam block is located at an intersection among the three major blocks (North China Craton, Yangtze Craton and Tarim Craton) in China (Fig. 1a).

This block consists of five nearly E-W trending subparallel tectonic units that were subsequently offset by the large Altyn-Tagh fault (e.g., Zhang et al., 2007; Song et al., 2012, 2013) (Fig. 1b). The Yushishan district is located at the junction of the Altyn-Tagh fault and Qilian block (Fig. 1b). Recently, two Nb-Ta rare metal deposits have been found: the Yushishan deposit and the Yushishanxi deposit (Fig. 2), which in total host >200 000 t of $Nb_2O_5$ and $Ta_2O_5$ minable resources (Yu et al., 2015).

Host rocks of the deposits are mainly the Mesoproterozoic Aoyougou Formation in the central part, which comprises low-grade metamorphic volcanic rocks, leptynite, leptite and carbonates. The Yushishan district has undergone strong multistage shearing and deformation by a series of EW-, NE-, and NEE-trending fractures (Yu et al., 2015; Jia, 2016). Diverse magmatic events occurred in this region at different times. The Paleozoic granitoids can be subdivided into two groups: the first is the early Paleozoic monzogranite, granodiorite, aegirine-augite syenite and syenite in the central part of the district; The second is represented by late Paleozoic intermediate-felsic intrusive rocks in the southern part, including quartz diorite, tonalite, biotite monzogranite, and granodiorite.

In addition to these metamorphic volcanic and sedimentary rocks and granitoids, one leucogranite dike outcrop has been first discovered in the Yushishanxi mining area during our field investigation in 2017 (Fig. 2). This EW-striking leucogranite dike intruded into the Aoyougou Formation, with several meters wide and up to hundreds of meters long. The leucogranite yielded LA-ICP-MS zircon U-Pb age of ~497 Ma (our unpublished data). The petrography and mineralogy further show that

the leucogranite has relatively uniform mineralogy, consisting of plagioclase (25%-30%; An%=8-13), K-feldspar (20%-25%), quartz (35%-40%), tourmaline (3%-5%) (Fig. 3a) and accessory minerals (garnet, apatite, and zircon). Euhedral to subhedral tourmalines grains, up to 3 mm in diameter, are commonly disseminated in the leucogranite (Tur-$D_1$ and Tur-$D_2$) (Figs. 3 and 4). Locally, crosscutting quartz-tourmaline veins (Tur-Q) and tourmaline veinlets (Tur-$T_1$ and Tur-$T_2$) are observed within the leucogranite (Figs. 4-6).

## TOURMALINE FEATURES AND PARAGENESIS

Different types of tourmaline, especially the Tur-$D_2$ and Tur-$T_1$, show distinctive core-rim zoning trends and significant chemical variations (Figs. 3-6). The growth of tourmaline in the Yushishanxi leucogranite can be subdivided into four major generations: Generation-I tourmalines are represented by the Tur-$D_1$ and the core of the Tur-$D_2$, whereas the changing trends from Generation-II to III were recorded in zones from the mantle to the rim of the Tur-$D_2$, from the core to the rim of the Tur-Q, and from the core to the mantle of the Tur-$T_1$, respectively; Generation-IV occurs as the overgrowth rim on Tur-$T_1$ and Tur-$T_2$ in the tourmaline veinlets.

The Tur-$D_1$ is homogeneously disseminated throughout the leucogranite and records the formation of Generation-I (Fig. 3a). The euhedral to subhedral tourmaline generally occurs as inclusions within the K-feldspar or plagioclase, and/or is filled interstitially by plagioclase, K-feldspar, and quartz (Figs. 3b-d). The precipitation of Tur-$D_1$ is nearly at the same time to these igneous minerals. Backscattered electron

153 (BSE) imaging shows the tourmaline has a slightly dark core and a narrow light rim
154 (Figs. 3c-d).

155 In the Tur-$D_2$, the oscillation-zoned overgrowth domains grew on corroded nuclei
156 of an earlier, dark green generation of tourmaline (Fig. 4b). Both BSE images and
157 X-ray elemental maps consistently show that the compositional variation parallels the
158 kinked trends, with the Fe contents decreasing abruptly from core to mantle, and then
159 increasing towards the rim (Figs. 4e-f). The core of the Tur-$D_2$ has similar
160 geochemical compositions to that of the Tur-$D_1$ (Fig. 3c-d and 4c), representing an
161 early generation (Generation-I). In contrast, the increasing Mg features from the
162 mantle to the rim (Generation-II to III) in Tur-$D_1$ (Figs. 4c-f) are consistent with that
163 of tourmalines from the core to the rim in the Tur-Q, and from the core to the mantle
164 in the Tur-$T_1$, respectively (Figs. 5-6).

165 In the outcrop, tourmaline-quartz (Tur-Q) veins (5-8 mm in width) are randomly
166 observed to crosscut the leucogranite (Fig. 5a-b). Tourmaline veinlets mainly occur
167 along cracks and fractures of the leucogranite and crosscut the leucogranite (Fig. 6a).
168 The early medium-grained zoned tourmaline (Tur-$T_1$) is surrounded by later
169 fine-grained tourmaline aggregates (Tur-$T_2$) (Figs. 6b-d). Although the genetic
170 relationship between the tourmaline-quartz veins and tourmaline veinlets could not be
171 unambiguously established due to a lack of enough field exposure, the overlap of
172 chemical variations between the core-rim in Tur-Q (Figs. 5e-f) and the core-mantle in
173 Tur-$T_1$ (Figs. 6e-f) indicates that tourmaline-quartz veins may form simultaneously or
174 earlier than the tourmaline veinlets and record the tourmaline growth of Generation-II

and III. Furthermore, in tourmaline veinlets, the sharply increasing Mg towards the rim in the Tur-$T_1$ is consistent with the high Mg signatures of the Tur-$T_2$ (Figs. 6c-f), which may record another new hydrothermal generation (Generation-IV) .

## ANALYTICAL METHODS

Mineral compositions were determined at the State Key Laboratory of Geological Processes and Mineral Resources (GPMA), China University of Geosciences (Wuhan), with a JEOL JXA-8100 Electron Probe Micro Analyzer (EPMA) equipped with four wavelength-dispersive spectrometers (WDS). During the analysis, an accelerating voltage of 15 kV, a beam current of 20 nA, and a 1-μm-spot size were used to analyze mineral compositions. Data were corrected on-line using a modified ZAF (atomic number, absorption, fluorescence) correction procedure. The peak counting time was 10 s for Na, Mg, Al, Si, K, Ca, Fe, F, and 20 s for Ti and Mn. The background counting time was one-half of the peak counting time on the high- and low-energy background positions. The relative standard deviation (1σ) on reported values is typically <3% for most elements, except for Ti and Ca (<5%). The following standards were used: sanidine (K), pyrope garnet (Al), almandine (Fe), diopside (Ca, Mg), jadeite (Na), rhodonite (Mn), olivine (Si), rutile (Ti), and fluorite (F). BSE images of tourmalines were also obtained by EPMA with the same condition. During an accelerating voltage of 15 kV, a beam current of 10 nA and a 0 μm (max focus) spot size were used to produce the X-ray elemental mapping of tourmaline, and the dwell time is set to be 5 ms. Tourmaline structural formulae were calculated by normalizing to 15 cations apfu (atoms per formula unit) in the tetrahedral and octahedral sites (T+Y+Z) (Henry and Dutrow, 1996), based on the

general formula $XY_3Z_6T_6O_{18}(BO_3)_3V_3W$, where X = Na, Ca, K, vacancies; Y = Fe, Mg, Mn, Ti, Al; Z = Al, Mg; T = Si, Al; B = 3; V + W = OH + F = 4, and that all Fe is present as $Fe^{2+}$ (Tindle et al., 2002).

Boron-isotopic compositions of tourmaline were measured by using a RESOlution S-155 laser ablation system coupled to a Nu Plasma II multi-collector ICP-MS (LA-MC-ICP-MS) at GPMA. Analyses were carried out with a beam diameter of 50 μm and 10 Hz repetition rate. Both $^{11}B$ and $^{10}B$ signals were collected statically and simultaneously by two Faraday cups. The instrumental mass fractionation was calibrated using the standard-sample-standard bracketing method using the international tourmaline standard IAEA B4 ($\delta^{11}B$= -8.71‰, Tonarini et al., 2003) as the external standard. Instrumental mass fractionation (IMF) and analytical quality were assessed by replicate analyses of tourmaline reference materials dravite (HS#108796) and schorl (HS#112566) from the Harvard Mineralogical Museum (Dyar et al., 2001). The similarity of IMF values determined for the chemically distinct tourmaline standards demonstrate insignificant matrix effect, in agreement with previous work (e.g., Ribeiro da Costa et al., 2014). The dravite yields an average $\delta^{11}B$ value of -6.4 ± 0.4‰ (1SD, n=9) and the schorl gives an average $\delta^{11}B$ value of -13.0 ± 0.3‰ (1SD, n=13) in this study, which are consistent with the reported values of -6.6 ± 0.1‰ and -12.5 ± 0.5‰ (Dyar et al., 2001). The analytical precision is estimated to be better than 0.5‰ based on replicate analyses of reference tourmalines during this study, and detailed analytical conditions and procedures can be seen in Zhao et al. (2019).

## RESULTS

### Chemical compositions of tourmaline

The major element compositions analyzed by EPMA and structural formulae of selected tourmaline are summarized in Table 1, and the full data set is present in Supplementary materials Appendix Table 1. Chemical compositions of tourmaline are described by different generations. Overall, the tourmaline samples show relatively large variations for MgO (1.35-9.73 wt%), FeO (2.17-15.23 wt%), $Al_2O_3$ (28.60-34.42 wt%), CaO (0.21-1.52 wt%), and $Na_2O$ (1.63-2.61 wt%), but small variations for $SiO_2$ (34.63-39.15 wt%), MnO (0-0.32 wt%), $TiO_2$ (0.03-2.14 wt%), and F (0-1.10 wt%). The $K_2O$ contents are generally low (<0.08 wt%), and $Cr_2O_3$ contents are below the detection limit.

Tourmaline analyses obtained from this study show overlapping concentrations of Na and Al, but there are distinctive patterns in Fe, Mg, and Ca. According to the classification of Henry et al. (2011), based on the X-site occupancy, all four tourmaline generations from Yushishanxi leucogranite belong to the alkali group (Fig. 7), with low vacancies in X-site (<0.39 apfu). Tourmaline compositions form distinct clusters in Al-Fe-Mg ternary diagrams of Henry and Guidotti (1985) (Fig. 8). The Generation-I and III tourmalines mainly plot in the field of Li-poor granitoids and associated pegmatites and aplites (field 2), while the Generation-II and IV tourmalines plot in the field of metapelites and metapsammites coexisting with an Al-saturating or poor phase (field 4 and 5) with several data points in the field of

243 $Fe^{3+}$-rich quartz-tourmaline rocks, calc-silicate rocks, and metapelites (field 6).

244 The tourmaline analyses from four generations all fall between the schorl
245 (Fe-rich) and dravite (Mg-rich) end member, with no significant uvite or feruvite
246 component (Fig. 9a). Generation-I and -III have low Mg/(Mg+Fe) (0.14-0.50 and
247 0.30-0.48, respectively) and high Na/(Na+Ca) (0.84-0.93 and 0.82-0.91, respectively)
248 ratios, and belong to the schorl. In contrast, Generation-II and IV have higher
249 Mg/(Mg+Fe) (0.51-0.80 and 0.55-0.88, respectively) and wider Na/(Na+Ca)
250 (0.66-0.94 and 0.75-0.93, respectively) ratios, and belong to dravite (Fig. 9a).
251 Generation-I has the highest Mn contents than the other three generations (Fig. 9b).
252 In the Mg versus Fe plot (Fig. 9c), all data show a linear relationship with a negative
253 slope of 1:1, which suggests that the main substitution vector in all samples is $MgFe_{-1}$.
254 Furthermore, the X-site vacancies and Y-site Al exhibit a positive correlation
255 decreasing from Generation-I to II (Figs. 9d-e), which is accordance with the foitite
256 $(Na, Mg)(^{X}\square, Al)_{-1}$ and olenite ($(Mg, OH)(Al, O)_{-1}$) substitution vectors. The
257 contribution of substitution vector $(Ca, Mg_2)(^{X}\square, Al_2)_{-1}$ can be used to explain the
258 weak increase in Ca from Generation-I to II (Fig. 9f). From Generation-III to IV, the
259 Mg and Al show an abrupt increase, which suggests the contributions of the foitite
260 $(Na, Mg)(^{X}\square, Al)_{-1}$ (Fig. 9f) besides $MgFe_{-1}$ (Fig. 9c).

261

262 **Boron-isotopic compositions of tourmaline**

263 Boron-isotopic compositions of tourmaline are listed in Appendix Table 2. The
264 total variation of $\delta^{11}B$ values for all generations of tourmaline is from -11.7‰ to

-6.0‰ (Fig. 10), which is well within the range reported for tourmalines from granites of various rock types and localities worldwide (Marshall and Jiang, 2011). In general, isotopic zonation is negligible for Tur-$D_1$, Tur-Q, and Tur-$T_2$, but is obvious for single crystals of Tur-$D_2$ (Fig. 4c) and Tur-$T_1$ (Figs. 6c). Tur-$D_2$ has a systematic $\delta^{11}B$ difference from -10.8‰ to -9.6‰ in the core, through -8.7‰ to -6.0‰ in the mantle, to -8.6‰ to -8.1‰ in the rim (Fig. 10a), which corresponds well to the elemental zones revealed by the BSE images and X-ray elemental maps. The boron-isotope compositions of Tur-$T_1$ from the tourmaline veinlets correspond to the compositional zonations, and become lighter over progressive growth zones, decreasing from -9.5‰ to -6.9‰ in the core, via -9.3‰ to -8.2‰ in the mantle, toward -11.1‰ to -9.8‰ in the rim (Fig. 10a). In summary, boron-isotopic compositions show an increase from Generation-I (-11.1‰ to -9.8‰) to II (-9.5‰ to -6.0‰) and III (-9.3‰ to -6.9‰), and then abruptly decrease toward Generation-IV (-11.7‰ to -9.8‰) (Figs. 10b).

## DISCUSSION

### Tourmaline compositional variations and implications for fluid evolution

The formation of tourmalines from Generation-I to IV is consistent with the compositional variations expected during a transition from B-rich melt to hydrothermal fluid. Generation-I tourmalines show characteristics similar to magmatic tourmaline previously reported by London and Manning (1995), such as relatively high Fe and Al contents and low Mg and Ca (Fig. 9). Typically, the Fe and

Mn contents in the Tur-$D_1$ show a slight enrichment from the cores toward the rims (Figs. 3c-d and 9), which is consistent with typical fractionation process of the highly evolved granites (e.g., Jiang et al., 2008; Duchoslav et al., 2017). In Al-Fe-Mg ternary diagram (Fig. 8), data for Generation-I tourmalines indicate they crystallized from a leucogranitic melt.

In contrast, the Generation-II tourmalines have distinct low Mn contents (Fig. 9b), which is consistent with the decreasing Mn during the transient from early magmatic to later hydrothermal processes. The generation-II of Tur-$D_2$ generally occurs as the oscillatory-zoning and overgrowth on the early Generation-I (Figs. 4c-f). Power (1968) described the occurrence of zoned acicular crystals of blue-green tourmaline that grew locally on corroded nuclei of an earlier, yellow-brown generation of tourmaline. From Generation-I to II tourmalines, the major elements (Mg and Ca) and boron isotopic compositions show an increasing trend which is clearly revealed in the core-mantle variations of Tur-$D_2$ (Figs. 4c and 9-10). In Al-Fe-Mg ternary diagram (Fig. 8), Generation-II tourmalines show more Mg-rich and Fe-poor signatures than Generation-I. In general, tourmaline associated with sedimentary and metamorphic rocks is commonly rich in Mg with variable amounts of Al and Ca, but tourmaline from granitic environments is typically rich in Fe (e.g., Henry and Guidotti, 1985; Morgan and London, 1989; Slack, 1996; Jiang et al., 2008; Baksheev et al., 2015). The significant increase of Mg/(Mg+Fe) ratios from Generation-I to II tourmalines (Figs. 4c and 9a) is probably related to the interaction of granitic magma-derived hydrothermal fluids with the surrounding

309 metasedimentary rocks. The regional Aoyougou Formation contains abundant
310 dolomitic marble and schists, which has the potential to supply Mg and Ca efficiently
311 to the fluid.

312 Generation-III tourmalines are characterized by strong concentric zoning with
313 overgrowth on the Generation-II (Figs. 4-6). As a whole, the BSE images, X-ray
314 elemental maps, and EPMA analyses uniformly show that the Fe contents increase
315 gradually from Generation-II to III. In contrast, the Mg contents follow a reverse
316 trend (Figs. 4-6 and 9a). Generation-III tourmalines have intermediate Fe/Mg values
317 (1.1-2.3) and in Fig. 8, the data significantly overlap with the area defined by
318 Generation-I tourmaline. This decrease in Mg/(Mg+Fe) ratios from Generation-II to
319 III (Figs. 4-6 and 8) can be attributed to a recharge of the magma-derived Fe-rich
320 hydrothermal fluid during magmatic-hydrothermal evolution (e.g., Duchoslav et al.,
321 2017). Compared with Generation-I, Generation-III tourmalines have relatively
322 higher Mg and Ca (Figs. 9c and f). This may be related to the crystallization phase
323 (melt/fluid) and also the possible influx of external fluids. Generation-I tourmalines
324 have a magmatic origin; thus, their compositions is strictly controlled by the granitic
325 melt. In contrast, Generation-III tourmalines are considered to be of hydrothermal
326 origin, and the hydrothermal fluids in equilibrium with them are dominated by the
327 proportion of magma-derived Fe-rich hydrothermal fluid and some residual external
328 Mg-rich fluids.

329 Generation-IV tourmalines in the veinlets commonly occur as the overgrowth
330 rim of the Tur-$T_1$ tourmaline (Figs. 6b-c) or as the fine-grained crystals (Tur-$T_2$; Fig.

6d). Compositionally, Generation-IV tourmalines have the highest Mg and the lowest Fe contents (Fig. 9). The increase of Mg/(Mg+Fe) ratios (Figs. 6c and 9a) and Al contents (Fig. 9e; Appendix Table 1) from Generation-III to IV may result from the influx of an external fluid from the surrounding metasedimentary rocks (i.e., Aoyougou Formations leptynite) into the hydrothermal fluid system. Multistage metamorphism and deformation events and the presence of abundant metamorphic rocks in the region (Yu et al., 2015; Jia, 2016) make it possible that Mg-rich metamorphic fluids circulate into the magmatic-hydrothermal fluid system, as is also supported by decreasing boron-isotope compositions from core to rim in the Tur-$T_1$ tourmaline (Fig. 6c).

**B-isotope heterogeneity and implications for multiple fluid sources**

The first-order feature of tourmaline from the Yushishanxi leucogranite is that the boron-isotopic compositions (-11.7 to -6.0 ‰) of all types of tourmaline are within the range of peraluminous S-type granites (-20‰ to -0‰) (Trumbull and Slack, 2018). Particularly, there exists evident heterogeneity of B-isotopic compositions at the scale of individual samples, locally even within single crystals, e.g., Tur-$D_2$ and Tur-$T_1$ (Figs. 4c, 6c and 10a). Isotopic heterogeneity at mineral scale may reflect the involvement of isotopically distinct multiple sources into the site of tourmaline growth during a single or multiple events (e.g., Palmer and Slack, 1989; Jiang et al., 2008; Krienitz et al., 2008; Pal et al., 2010). So far, no direct experimental studies exist on B-isotopic fractionation between melt and tourmaline, but since $^{11}B$ is

353 preferentially portioned into tourmaline and aqueous fluids, both crystallization of
354 tourmaline and exsolution of an aqueous fluid phase would deplete the remaining
355 magma in $^{11}B$. In this study, we follow an approach to calculating fractionation
356 between melt-fluid (Hervig et al., 2002) and tourmaline-fluid (Marschall et al., 2009;
357 Meyer et al., 2008) on the hypothesis of an equal proportion of trigonal and
358 tetrahedral B in the melt (cf. Kaliwoda et al., 2011; Trumbull et al., 2013).

359 The earliest magmatic Generation-I tourmalines have relatively homogeneous
360 boron-isotopic compositions with an average value of -10.4‰ (Fig.10b). Due to the
361 lack of precise thermometric data, we assume the formation temperature of
362 Generation-I tourmaline was 650 $^{o}$C according to the experimental study for the
363 tourmaline stability in leucogranite magma (Scaillet et al., 1995). The combined
364 fractionation factors between melt and tourmaline using data from Meyer et al. (2008)
365 and Hervig et al. (2002) are -2.8‰ at 650 $^{o}$C. This would imply that the $\delta^{11}B$ value of
366 the initial melt from which the Generation-I tourmalines crystallized is around
367 -13.2‰.

368 With progressive fractional crystallization and decrease of temperature,
369 hydrothermal fluids will exsolve from the granitic melt. Considering that fluid
370 exsolution can occur at a wide range of temperatures and pressures (e.g., Candela,
371 1997), it is hard to precisely know the temperature from which the hydrothermal fluid
372 may exsolve. To better constrain isotope-fractionation processes, we assumed the
373 hydrothermal fluid from which Generation-II crystallized was at relatively wide
374 temperature ranges from 600 $^{o}$C to 450 $^{o}$C. During tourmaline crystallization from a

375 fluid media, $^{10}B$ partitions preferentially into tourmaline, with a tourmaline-fluid
376 fractionation factor of $\Delta^{11}B_{Tur\text{-}fluid}$ = -1.3 to -2.3 ‰ (hypothetical $T$ = 600-450 °C)
377 (Meyer et al., 2008). Based on the average $\delta^{11}B$ value (-7.8‰) of Generation-II, the
378 B-isotope fractionation between granite melt and fluid is calculated to be 5.7 to 4.2‰
379 at 600-450 °C. If the hydrothermal fluids directly exsolved from granitic magma, the
380 $\delta^{11}B$ values would be of -7.5 to -9.0‰. Indeed, they are relatively lower than the
381 ranges of hydrothermal fluids from which Generation-II crystallized. However, model
382 calculation indicates that a higher $\delta^{11}B$ value of -6.5‰ at 600 °C can be achieved
383 during progressive fractionation when 83.7% of the boron is removed from the fluid
384 (i.e., F=0.143) (Fig. 11a); the boron-isotopes of -5.5‰ at 450 °C of the hydrothermal
385 fluid can be achieved by the removal of 58.4% of the boron from the fluid (Fig. 11b).
386 Thus, the boron-isotopic variations between Generation-I and II may result from the
387 Rayleigh fractionation process.

388 The boron-isotopic composition of Generation-III tourmaline has an average
389 $\delta^{11}B$ of -8.3‰ and is slightly lighter than Generation-II tourmaline (Fig. 10b). This
390 weak contrast between Generation-II and III may not be sufficient to distinguish if
391 this represents a granite-derived fluid affected by fractionation processes in
392 association with fluid exsolution and temperature decrease during hydrothermal
393 evolution, or if there was a mixing of heavier boron from an additional fluid.
394 However, the increasing Fe in Generation-III tourmaline revealed from BSE images,
395 X-ray elemental maps, and EPMA analyses (Figs. 4-6 and 8a) supports the latter
396 interpretation. The most reasonable explanation for the shift from Generation-II to III

397 is a recharge of the initial Fe-rich hydrothermal fluid derived from granitic magma.

398 Compared with the other three generations, Generation-IV and especially Tur-$T_2$
399 in the tourmaline veinlets have the lowest $\delta^{11}B$ values (down to -11.7‰) (Figs. 6c and
400 10b; Appendix Table 2). Indeed, Rayleigh fractionation can produce much larger
401 variations in isotopic compositions; however, the model predicts progressively
402 heavier isotopic compositions of later generation tourmaline, which is contrary to the
403 observed differences from Generation-III to IV. Therefore, we can first exclude the
404 effect of Rayleigh fractionation on boron-isotopic variations. Considering that no
405 thermometric data can be available, we assume that Generation-III (e.g., 400 $^{o}$C)
406 formed at temperature 150 $^{o}$C higher than Generation-IV tourmaline (e.g., 250 $^{o}$C).
407 The average $\delta^{11}B$ values of corresponding fluid for Generation-III and IV are
408 calculated to be -5.6‰ and -6.2‰, respectively, which may have limited variations
409 but also within the analytical error. Although we could not rule out the temperature
410 impact on B isotopes, the significant lower $\delta^{11}B$ values and Mg- and Al-rich
411 signatures (Figs. 6 and 9-10) of Generation-IV tourmalines provide further evidence
412 for the involvement of an isotopically light external fluid in their formation. In the
413 Yushishan district, the regional metamorphosed volcanic and sedimentary successions
414 (e.g., leptynite, amphibolite, marble in Aoyougou Formation) experienced strong
415 metamorphism (Yu et al., 2015; Jia, 2016). The breakdown of mica in the
416 surrounding rocks during regional upper amphibolite facies metamorphism may
417 provide the possibility for light boron source (e.g., Wunder et al., 2005; Sievers et al.,
418 2017; Albert et al., 2018). A cartoon is used to illustrate the formation of multiple

generation tourmalines in the Yushishanxi leucogranite and boron isotopic variations from magmatic to hydrothermal stages (Fig. 12).

## IMPLICATIONS FOR THE ZONED TOURMALINE

The zoned tourmalines, in particular, are useful petrogenetic indicators of magmatic and magmatic-hydrothermal evolution, and their geochemistry has long been used to track the history of magmatic-hydrothermal processes (e.g., Jiang et al., 2008; Yu et al., 2017; Codeço, et al., 2017; Zhao et al., 2019). In this study, we present an excellent example with five distinct types of tourmaline from the leucogranite dike in the Yushishanxi mining area. Some of the tourmaline grains exhibit obvious core-rim zonation, especially the Tur-$D_2$ and Tur-$T_1$. Detailed petrographic, geochemical, and isotopic studies reveal four major generations of tourmaline growth, as shown in the cartoon diagram (Fig. 12), which record a complex formation history from B-rich melt to hydrothermal fluid. The boron-isotope fractionation is also discussed through the Generation-I to IV tourmalines, which attributed to the fractionation between melt-fluid, tourmaline-fluid, and Rayleigh fractionation, as well as recharge of magma-derived Fe-rich hydrothermal fluids and mixing of external fluids with B release during mica breakdown within the surrounding metamorphic rocks. Such a process may have happened in many different occurrences worldwide, and therefore there is a need to carry out a detailed study on the secular changes of geochemical and boron-isotopic compositions of tourmaline to unravel the evolutionary history for the magmatic and hydrothermal

441 processes involved during tourmaline formation. Additionally, in the Yushishanxi
442 mining area, the Nb- and Ta-bearing minerals are mainly distributed in the leptynite,
443 which suggests that the Nb-Ta mineralization may be linked to hydrothermal
444 processes. Although the genetic relationship between the Nb-Ta mineralization and
445 leucogranite is not clear, the presence of external fluids during crystallization
446 differentiation revealed from tourmaline study do suggest these fluid mixing
447 processes may change the physic-chemical factors and lead to the Nb and Ta
448 precipitation in the leptynite. In summary, a complex natural magmatic system
449 coupled with field, textural, and mineral evidence of difference evolutionary stages
450 has great potential to yield distinct morphological and geochemical features of their
451 origin. Multi-generation crystallization and chemical variations in zoned tourmaline
452 grains can provide valuable information regarding the complex formation history of
453 magmatic and metamorphic reactions, fluid provenance and evolution, and
454 petrogenesis.
455

456 **ACKNOWLEDGEMENTS**

457 This work was financially supported by projects from the Ministry of Science
458 and Technology (MOST) National Key R&D Program of China (No.
459 2017YFC0602405) and the MOST Special Fund from the State Key Laboratory of
460 Geological Processes and Mineral Resources, China University of Geosciences (No.
461 MSFGPMR03-2). We thank Dr. Kui-dong Zhao, Wei Chen, and Shui-yuan Yang for
462 their help during LA-MC-ICP-MS and EMPA analysis. We are grateful to Dr. Don R.

Baker, Fang-zhen Teng, Marta S. Codeço, and two anonymous reviewers for their thorough and constructive comments and suggestions, which significantly improved an earlier draft of this manuscript.

## Appendix A. Supplementary data

Supplementary data associated with this article can be found, in the online version.

## REFERENCES CITED

Baksheev, I.A., Prokofiev, V.Y., Trumbull, R.B., Wiedenbeck, M., and Yapaskurt, V.O. (2015) Geochemical evolution of tourmaline in the Darasun gold district, Transbaikal region, Russia: Evidence from chemical and boron isotopic compositions. Mineralium Deposita, 50(1), 125-138.

Bénard, F., Moutou, P., and Pichavant, M. (1985) Phase relations of tourmaline leucogranites and the significance of tourmaline in silicic magmas. Journal of Geology, 93, 271-291.

Buriánek, D., and Novák, M. (2007) Compositional evolution and substitutions in disseminated and nodular tourmaline from leucocratic granites: Examples from the Bohemian Massif, Czech Republic. Lithos, 95, 148-164.

Candela, P. A. (1997) A review of shallow, ore-related granites: textures, volatiles, and ore metals. Journal of Petrology, 38, 1619-1633.

Codeço, M.S., Weis, P., Trumbull, R.B., Glodny, J., Wiedenbeck, M., and Romer, R.L.

(2019) Boron isotope muscovite-tourmaline geothermoetry indicates fluid cooling during magmatic-hydrothermal W-Sn ore formation. Economic Geology, 114, 153-163.

Codeço, M.S., Weis, P., Trumbull, R.B., Pinto, F., Lecumberri-Sanchez, P., and Wilke, F.D.H. (2017) Chemical and boron isotopic composition of hydrothermal tourmaline from the Panasqueira W-Sn-Cu deposit, Portugal. Chemical Geology, 468, 1-16.

Dingwell, D.B., Romano, C., and Hess, K.U. (1996) The effect of water on the viscosity of a haplogranitic melt under P-T-X conditions relevant to silicic volcanism. Contributions to Mineralogy and Petrology, 124, 19-28.

Duchoslav, M., Marks, M.A.W., Drost, K., McCammon, C., Marschall, H.R., Wenzel, T., and Markl, G. (2017) Changes in tourmaline composition during magmatic and hydrothermal processes leading tin-ore deposition: the Cornubian Batholith, SW England. Ore Geology Review, 83, 215-234.

Dyar, M. D., Wiedenbeck, M., Robertson, D., Cross, L.R., Delaney, J.S., Ferguson, K., Francis, C.A., Grew, E.S., Guidotti, C.V., Hervig, R.L., Hughes, J.M., Husler, J., Leeman, W., McGuire, A.V., Rhede, D., Rothe, H., Paul, R.L., Richards, I., and Yates, M. (2001) Reference minerals for the microanalysis of light elements. Geostandards Newsletter, 25, 441-463.

Geisinger, K.L., Oestrike, R., Navrotsky, A., Turner, G.L., and Kirkpatrick, R.J. (1988) Thermochemistry and structure of glasses along the join $NaAlSi_3O_8$-$NaBSi_3O_8$. Geochimica et Cosmochimic Acta, 52, 2405-2414.

507 Hawthorne, F.C., and Dirlam, D.M. (2011) Tourmaline the indicator mineral: from
508 atomic arrangement to viking navigation. Element, 7, 307-312.
509 Henry, D.J., and Dutrow, B.L. (1996) Metamorphic tourmaline and its petrologic
510 applications. In: Grew, E.S., Anovitz, L.M. (Eds.), Boron: Mineralogy, Petrology
511 and Geochemistry. In: Review in Mineralogy, 33, 503-557.
512 Henry, D.J., and Dutrow, B.L. (2012) Tourmaline at diagenetic to low-grade
513 metamorphic condictions: Its petrologic applicability. Lithos, 154, 16-32.
514 Henry, D.J., and Guidotti, C.V. (1985) Tourmaline as a petrogenetic indicator
515 mineral-an example from the staurolite-grade metapelites of NW
516 Maine. American Mineralogist, 70(1), 1-15.
517 Henry, D.J., Novák, M., Hawthorne, F.C., Ertl, A., Dutrow, B.L., Uher, P., and
518 Pezzotta, F. (2011) Nomenclature of the tourmaline-supergroup minerals.
519 American Mineralogist, 96, 895-913.
520 Hervig, R.L., Moore, G.M., Williams, L.B., Peacock, S.M., Holloway, J.R., and
521 Roggensack, K. (2002) Isotopic and elemental partitioning of boron between
522 hydrous fluid and silicate melt. American Mineralogist, 87, 769-774.
523 Jia, Z.L. (2016) Geochemical and metallogenetical characteristics of Nb-Ta-Rb
524 deposit, South Qilian-Beishan area, Gansu Province, China (Ph.D Dissertation),
525 Lanzhou University, China (in Chinese with English abstract).
526 Jiang, S.Y., and Palmer, M.R. (1998) Boron isotope systematic of tourmaline from
527 granites and pegmatites: a synthesis. European Journal of Mineralogy, 10(6),
528 1253-1265.

529 Jiang, S.Y., Palmer, M.R., and Yeats, C.J. (2002) Chemical and boron isotopic
530 compositions of tourmaline from the Archean Big Bell and Mount Gibson gold
531 deposits, Murchison Province, Yilgarn Craton, Western Australia. Chemical
532 Geology, 188(3-4), 229-247.
533 Jiang, S.Y., Radvanec, M., Nakamura, E., Palmer, M., Kobayashi, K., Zhao, H.X.,
534 and Zhao, K.D. (2008) Chemical and boron isotopic variations of tourmaline in
535 the Hnilec granite-related hydrothermal system, Slovakia: Constraints on
536 magmatic and metamorphic fluid evolution. Lithos, 106, 1-11.
537 Kaliwoda, M., Marschall, H.R., Marks, M.A.H., Ludwig, T., Altherr, R., and Markl, G.
538 (2011) Boron and boron isotope systematics in the peralkaline Iímaussaq
539 intrusion (South Greenland) and its granitic country rocks: A record of magmatic
540 and hydrothermal processes. Lithos, 125, 51-64.
541 Kowalski, P.M., Wunder, B., and Jahn, S. (2013) Ab-initio prediction of equilibrium
542 boron isotope fractionation between minerals and aqueous fluids at high P and T.
543 Geochimica et Cosmochimic Acta, 101, 285-301.
544 Krienitz, M.S., Trumbull, R.B., Hellmann, A., Kolb, J., Meyer, F.M., and Wiedenbeck,
545 M. (2008) Hydrothermal gold mineralization at the Hira Buddini gold mine,
546 India: constraints on fluid evolution and fluid sources from boron isotopic
547 compositions of tourmaline. Mineralium Deposita, 43(4), 421-434.
548 Li, N., Ulrich, T., Chen, Y.J., Thompson, T.B., Pease, V., and Pirajno, F. (2012) Fluid
549 inclusion of the Yuchiling porphyry Mo deposit, East Qinling, China. Ore
550 Geology Review, 48, 442-459.

551 London, D. (1999) Stability of tourmaline in peraluminous granite system: the boron
552 cycle from anatexis to hydrothermal aureoles. European Journal of Mineralogy,
553 11, 253-262.
554 London, D., and Manning D.A.C. (1995) Chemical variation and significance of
555 tourmaline from southwest England. Economic Geology, 90, 495-519.
556 London, D., Morgan, G.B., and Wolf, M.B. (1996) Boron in granitic rocks and their
557 contact aureoles. Reviews in Mineralogy, 33, 299-330.
558 Marschall, H.R., Altherr, R., Kalt, A., and Ludwig, T. (2008) Detrital, metamorphic
559 and metasomatic tourmaline in high-pressure metasediments from Syros
560 (Greece): intra-grain boron isotope patterns determined by secondary-ion mass
561 spectrometry. Contributions to Mineralogy and Petrology, 155(6), 703-717.
562 Marschall, H.R., and Jiang, S.Y. (2011) Tourmaline isotopes: no element left behind.
563 Elements, 7, 313-319.
564 Marschall, H.R., Ludwig, T., Altherr, R., Kalt, A., and Tonarini, S. (2006) Syros
565 metasomatic tourmaline: evidence for very high-$\delta^{11}$B fluids in subduction zones.
566 Journal of Petrology, 47(10), 1915-1942.
567 Meyer, C., Wunder, B., Meixner, A., Romer, R.L., and Heinrich, W. (2008)
568 Boron-isotope fractionation between tourmaline and fluid: an experimental
569 re-investigation. Contributions to Mineralogy and Petrology, 156, 259-267.
570 Mlynarczyk, M.S.J., and Williams-Jones, A.E. (2006) Zoned tourmaline associated
571 with cassiterite: Implications for fluid evolution and tin mineralization in the
572 San Rafael Sn-Cu deposit, Southeastern Peru. Canadian Mineralogist, 44,

347-365.

Morgan, G.B., London, D. (1989) Experimental reactions of amphibolites with boron-bearing aqueous fluids at 200 Mpa: implications for tourmaline stability and partial melting in mafic rocks. Contributions to Mineralogy and Petrology, 102, 281-297.

Pal, D.C., Trumbull, R.B., and Wiedenbeck, M. (2010) Chemical and boron isotope compositions of tourmaline from the Jaduguda U (-Cu-Fe) deposit, Singhbum shear zone, India: Implications for the source and evolution of mineralizing fluids. Chemical Geology, 277, 245-260.

Palmer, M.R., London, D., Morgan, G.B. VI, and Babb, H.A. (1992) Experimental determination of fractionation of $^{11}B/^{10}B$ between tourmaline and aqueous vapor: a temperature- and pressure-dependent isotopic system. Chemical Geology, 101, 123-129.

Palmer, M.R., and Slack, J.F. (1989) Boron isotopic composition of tourmaline from massive sulphide deposits and tourmalinites. Contributions to Mineralogy and Petrology, 103, 434-451.

Palmer, M.R., and Swihart, G.H. (1996) Boron isotope geochemistry: an overview. In: Review in Mineralogy, 33, 709-744.

Power, G.M. (1968) Chemical variation in tourmalines from south-west England. Mineralogical Magazine, 36, 1078-1089.

Ribeiro da Costa, I., Mourao, C., Recio, C., Guimaraes, F., Antunes, I.M., Farinha Ramos, J., Barriga, F.J.A.S., Palmer. M.R., and Milton, J.A. (2014) Tourmaline

595 occurrences within the Penamacor-Monsanto granitic pluton and host-rocks
596 (Central Portugal): Genetic implications of crystal-chemical and isotopic
597 features. Contributions to Mineralogy and Petrology, 167, 993-1016.
598 Scaillet, B., Pichavant, M., and Roux, J. (1995) Experimental crystallization of
599 leucogranite magmas. Journal of Petrology, 36(3), 663-705.
600 Siegel, K., Wagner, T., Trumbull, R.B., Jonsson, E., Matalin, G., Wälle, M., and
601 Heinrich, C.A. (2016) Stable isotope (B, H, O) and mineral-chemistry
602 constraints on the magmatic to hydrothermal evolution of the Varuträsk
603 rare-element pegmatite (Northern Sweden). Chemical Geology, 421, 1-16.
604 Sievers, N.E., Menold, C.A., Grove, M., and Coble, M.A. (2017) White mica trace
605 element and boron isotope evidence for distinctive infiltration events during
606 exhumation of deeply subducted continental crust. International Geology
607 Review, 59 (5-6), 621-638
608 Sinclair, W.D., and Richardson, J.M. (1992) Quartz-tourmaline orbicules in the
609 Seagull batholith, Yukon Territory. Canadian Mineralogist, 30, 923-935.
610 Slack, J.F. (1996) Tourmaline associations with hydrothermal ore deposit. Reviews in
611 Mineralogy and Geochemistry, 33, 559-643.
612 Smith, M.P., and Yardley, B.W.D. (1996) The boron isotopic composition of
613 tourmaline as a guide to fluid processes in the southwestern England Orefield:
614 An ion microprobe study. Geochimica et Cosmochimica Acta, 60, 1415-1427.
615 Song, S.G., Niu, Y.L., Su, L., and Xia, X.H. (2013) Tectonics of the North Qilian
616 orogen, NW China. Gondwana Research, 23, 1378-1401.

617 Song, S.G., Su, Li., Li, X.H., Niu, Y.L., and Zhang, L.F. (2012) Grenville-age
618 orogenesis in the Qaidam-Qilian block: The link between South China and
619 Tarim. Precambrian Research, 220-221, 9-22.
620 Tindle, A.G., Breaks, F.W., Selway, J.B. (2002). Tourmaline in petalite-subtype ranitic
621 pegmatites: evidence of fractionation and contamination from the Pakeagama
622 Lake and separation Lake areas of northwestern Ontario, Canada. Canadian
623 Mineralogist, 40, 753-788.
624 Tonarini, S., Pennisi, M., Adorni-Braccesi, A., Dini, A., Ferrara, G., Gonfiantini, R.,
625 Wiedenbeck, M., and Gröning, M. (2003) Intercomparison of boron isotope and
626 concentration measurements. Part I: Selection, preparation and homogeneity
627 tests of the intercomparison materials. Geostandards and Geoanalytical
628 Research, 27, 21-39.
629 Trumbull, R.B., Beurlen, H., Wiedenbeck, M., and Soares, D.R. (2013) The diversity
630 of B-isotope variations in tourmaline from rare-element pegmatites in the
631 Borborema Province of Brazil. Chemical Geology, 352, 47-62.
632 Trumbull, R.B., and Chaussidon, M. (1999) Chemical and boron isotopic
633 composition of magmatic and hydrothermal tourmalines from the Sinceni
634 granite-pegmatite system in Swaziland. Chemical Geology, 153(1-4), 125-137.
635 Trumbull, R.B., Krienitz, M.S., Gottesmann, B., and Wiedenbeck, M. (2008)
636 Chemical and boron -isotope variations in tourmalines from an S-type granite
637 and its source rocks: the Erongo granite and tourmalines in the Damara Belt,
638 Namibia. Contributions to Mineralogy Petrology, 155, 1-18.

639 Trumbull, R.B., Slack, J.F. (2018) Boron isotopes in the continental crust: granites,
640 pegmatites, felsic volcanic rocks, and related ore deposits. In: Marschall, H.,
641 Foster, G. (Eds), Boron Isotopes: The Fifth Element, Springer, Switzerland,
642 249-272.
643 Trumbull, R.B., Codeço, M.S., Jiang, S.Y., Palmer, M.R., and Slack, J.F. (2020)
644 Boron isotope variations in tourmaline from hydrothermal ore deposits: a review
645 of controlling factors and insights for mineralizing systems. Ore Geology
646 Reviews, Doi: https://doi.org/10.1016/j.oregeorev.2020.103682.
647 van Hinsberg, V.J., Henry, D.J., and Marschall, H.R. (2011) Tourmaline: an ideal
648 indicator of its host environment. Canadian Mineralogist, 49, 1-16.
649 von Goerne, G., Franz, G., and Wirth, R. (1999) Hydrothermal synthesis of large
650 dravite crystals by the chamber method. European Journal of Mineralogy, 11,
651 1061-1078.
652 Wunder, B., Meixner, A., Romer, R.L., Wirth, R., and Heinrich, W. (2005) The
653 geochemical cycle of boron: Constraints from boron isotope partitioning
654 experiments between mica and fluid. Lithos, 84, 206-216.
655 Xiu, Q.Y., Yu, H.F., Li, Q., Zuo, G.C., Li, J.W., and Cao, C.J. (2004) Discussion on
656 the petrogenic time of Longshoushan Group, Gansu Province. Acta Geologica
657 Sinica, 78, 366-373 (in Chinese with English abstract).
658 Yang, S.Y., and Jiang, S.Y. (2012) Chemical and Boron isotopic composition of
659 tourmaline in the Xiangshan volcanic-intrusive complex, Southest China:
660 Evidence for boron mobilization and infiltration during magmatic-hydrothermal

process. Chemical Geology, 312-313, 177-189.

Yang, S.Y., Jiang, S.Y., and Palmer, M.R. (2015) Chemical and boron isotopic compositions of tourmaline from the Nyalam leucogranites, South Tibetan Himalaya: Implication for their formation from B-rich melt to hydrothermal fluids. Chemical Geology, 419, 102-113.

Yu, J.P., Wu, Y.B., Liang, M.H., Xiao, P.X., and Dou, X.Y. (2015) New progress of the southern Altyn Tagh geological mapping and guide the prospecting support: according to 1:50000 Mobeier and other five regional geological maps in Gansu Province. Geological Survey of China, 2, 40-47 (in Chinese with English abstract).

Yu, M., Feng, C.Y., Mao, J.W., Zhao, Y.M., and Li, D.X. (2017) Multistage skarn-related tourmaline from the Galinge deposit, Qiman Tagh, Western China: A fluid evolution perspective. Canadian Mineralogist, 55, 3-19.

Zhang, J.X., Meng, F.C., and Wan, Y.S. (2007) A cold Early Palaeozoic subduction zone in the North Qilian Mountains, NW China: petrological and U-Pb geochronological constrains. Journal of Metamorphic Geology, 25, 285-304.

Zhang, J.X., Yu, S.Y., Li, Y.S., Yu, X.X., Lin, Y.H., and Mao, X.H. (2015) Subduction, accretion and closure of Proto-Tethyan Ocean: Early Paleozoic accretion/collision orogeny in the Altun-Qilian-North Qaidam orogenic system. Acta Petrologica Sinica, 31(12), 3531-3554.

Zhao, H.D., Zhao, K.D., Palmer, M.R., and Jiang, S.Y. (2019) In-situ elemental and boron isotopic variations of tourmaline from the Sanfang granite, South China:

683 Insights into magmatic-hydrothermal evolution. Chemical Geology, 504,
684 190-204.

685

686

687

688 # Table captions

689 **TABLE 1**. A summary of EPMA data of tourmaline from the Yushishanxi leucogranite.

690

691 # Figures captions

692 **FIGURE 1. (a)** Tectonic framework of China, showing the location of the Qilian
693 block (modified from Li et al., 2012); **(b)** Geologic map of the Qilian block and the
694 location of Yushishan district (modified from Zhang et al., 2015 and Song et al.,
695 2013). Abbreviation: Qaidam Basin (QDB), Qilian block (QL), Central China
696 Orogeny (CCO), North Qilian orogenic belt (NQL), North Altun
697 subduction-accretion complex belt (NAT), Central Altun block (CAB), South Altun
698 subduction-collision complex belt (SAT), North Qaidam continental-type UHPM belt
699 (NQD).

700

701 **FIGURE 2.** Local geologic map of the Yushishan district, showing the location of
702 Yushishanxi Nb-Ta deposit.

703

704 **FIGURE 3.** Photographs of the fine-grained disseminated tourmaline (Tur-$D_1$ type)
705 in the leucogranite. (a) Hand specimen of the Tur-$D_1$; (b) Photomicrographs of
706 euhedral and subhedral Tur-$D_1$ surrounded by the K-feldspar; (c-d) BSE images of
707 Tur-$D_1$ in the leucogranite, with a respectively homogeneous core and a narrow zoned
708 rim. The red circles are the points of the EPMA analyses, with the attached
709 Mg/(Mg+Fe) ratios. The light blue circles are the points of the LA-MC-ICP-MS

boron isotope analyses, with the attacted $\delta^{11}B$ values (in ‰). Abbreviations: tourmaline (Tur), quartz (Qz), plagioclase (Pl), K-feldspar (Kfs), Generation (Gen).

**FIGURE 4.** Photographs of the medium-coarse grained zoned tourmaline (Tur-$D_2$ type) in the leucogranite. **(a)** Hand specimen of the Tur-$D_2$; **(b)** Zoned Tur-$D_2$ crystal exhibits clear pleochroism from dark green to yellowish-brown; **(c)** BSE image of Tur-$D_2$ showing obvious compositional zoning, from bright in the core through pale in the mantle to light in the rim; **(d)** BSE image of Tur-$D_2$ show that early Fe-rich cores was cut and overprinted by later Mg-rich tourmalines; **(e-f)** X-ray element maps of Fe and Mg for the Tur-$D_2$. The red circles are the points of the EPMA analyses, with the attached Mg/(Mg+Fe) ratios. The light blue circles are the points of the LA-MC-ICP-MS boron isotope analyses, with the attacted $\delta^{11}B$ values (in ‰). Abbreviations: tourmaline (Tur), quartz (Qz), plagioclase (Pl), Generation (Gen).

**FIGURE 5.** Photographs of tourmalines in tourmaline-quartz vein (Tur-Q type). **(a)** Hand specimen of Tur-Q crosscutting leucogranite; **(b)** Photomicrographs of tourmaline-quartz vein crosscutting leucogranite; **(c-d)** BSE images of Tur-Q showing obvious compositional zoning, from pale core to bright rim; **(e-f)** X-ray element maps of Fe and Mg for the Tur-Q. The red circles are the points of the EPMA analyses, with the attached Mg/(Mg+Fe) ratios. The light blue circles are the points of the LA-MC-ICP-MS boron isotope analyses, with the attacted $\delta^{11}B$ values (in ‰). Abbreviations: tourmaline (Tur), quartz (Qz), plagioclase (Pl), K-feldspar (Kfs),

732 Generation (Gen).

733

734 **FIGURE 6.** Photographs of tourmalines in tourmaline veinlets. **(a)** Hand specimen;
735 **(b)** Photomicrographs of medium-grained zoned tourmaline (Tur-$T_1$ type) and
736 fine-grained tourmaline aggregates (Tur-$T_2$ type) in tourmaline veinlets; **(c-d)** BSE
737 images showing that Tur-$T_1$ has obvious compositional zoning from pale core
738 through bright mantle to ash black rim, but the Tur-$T_2$ is homogeneous without
739 obvious zoning; **(e-f)** X-ray element maps of Fe and Mg for the Tur-$T_1$. The red
740 circles are the points of the EPMA analyses, with the attached Mg/(Mg+Fe) ratios.
741 The light blue circles are the points of the LA-MC-ICP-MS boron isotope analyses,
742 with the attacted $\delta^{11}B$ values (in ‰). Abbreviations: tourmaline (Tur), quartz (Qz),
743 Generation (Gen).

744

745 **FIGURE 7.** Classification diagrams of all types of tourmalines from the Yushishanxi
746 leucogranite based on X-site occupancy (after Henry et al., 2011).

747

748 **FIGURE 8.** Ternary Al-Fe-Mg diagram showing compositional variations of
749 tourmaline from the Yushishanxi leucogranite. The regions define the compositions of
750 tourmaline from different rock types, according to Henry and Guidotti (1985).
751 1=Li-rich granitoids and associated pegmatites and aplites; 2=Li-poor granitoids and
752 associated pegmatites and aplites; 3=$Fe^{3+}$-rich quartz-tourmaline rocks
753 (hydrothermally altered granites); 4=Metapelites and metapsammites coexisting with

754 an Al-saturating phase; 5=Metapelites and metapsammites not coexisting with an
755 Al-saturating phase; 6=$Fe^{3+}$-rich quartz-tourmaline rocks, calc-silicate rocks, and
756 metapelites; 7=Low Ca metaultramafics and Cr, V-rich metasediments;
757 8=Metacarbonates and metapyroxenites.
758
759 **FIGURE 9. (a)** Tourmaline subtypes based on the classification diagram of
760 Mg/(Mg+Fe) versus Na/(Na+Ca). **(b)** Plot of Mg/(Mg+Fe) versus Mn, showing the
761 Tur-$D_1$ and the core of the Tur-$D_1$ have higher Mn contents. **(c)** Plot of Mg versus Fe,
762 showing all of the tourmaline samples have strong substitution of $MgFe_{-1}$. **(d-f)** Plots
763 of Na versus X-site vacancy, Al tot versus X-site vacancy and Mg versus Ca with
764 common exchange vector, showing the substitution of $MgFe_{-1}$, $((Na, Mg)(^{X}\square, Al)_{-1}$
765 and $(Ca, Mg_2)(^{X}\square, Al_2)_{-1}$ for tourmalines from the Yushishanxi leucogranite. All
766 values are in atoms per formula unit (apfu).
767
768 **FIGURE 10. (a)** B-isotopic compositions for five distinctive types. **(b)** Histograms
769 of four generations tourmaline from the Yushishanxi leucogranite. The gray boxes
770 mark the 25th (P1) and 75th percentiles (P1); the black line and filled circles
771 represent the median and average, respectively; the whiskers represent the range.
772
773 **FIGURE 11.** Boron isotope fractionation models between tourmaline and aqueous
774 fluid (after Marschall et al., 2009, using fractionation values from Meyer et al., 2008),
775 and assuming a fluid temperature of 600 and 450 $^{o}$C. **(a)** initial $\delta^{11}B_{fluid}$ of -8.2‰, **(b)**

776 initial $\delta^{11}B_{fluid}$ of -7.5‰.

777

778 **FIGURE 12.** A summary cartoon showing the formation of multiple generation
779 tourmalines and boron-isotopic variations during the late magmatic to hydrothermal
780 evolution of the Yushishanxi leucogranite. Five types of tourmaline in the Yushishan
781 leucogranite have been observed in the field, which can be subdivided into four
782 generations, including magmatic Generation-I and hydrothermal Generation-II, III
783 and IV. The Mg/(Mg+Fe) (abbreviated as Mg#) increase from Generation-I to
784 Generation-II, then decrease to Generation-III, and finally increase towards
785 Generation-IV. The boron-isotopic compositions show a kinked trend that increase
786 from Generation-I to Generation-II, and then decrease towards Generation-III and V.
787 The complex formation history may happen regarding boron fractionation between
788 the melt-fluid, tourmaline-fluid and Rayleigh fractionation, as well as recharge of
789 magma-derived Fe-rich hydrothermal fluids and mixing of an Mg- and Al-rich and
790 B-light external fluid during mica breakdown within the surrounding metamorphic
791 rocks.

792

793 ## Supplementary Appendix Tables

794 **Appendix Table 1.** EPMA data of tourmaline from the Yushishanxi leucogranite.

795

796 **Appendix Table 2.** LA-MC-ICP-MS boron isotope data of tourmaline from the Yushishanxi
797 leucogranite.

This is the peer-reviewed, final accepted version for American Mineralogist, published by the Mineralogical Society of America.
The published version is subject to change. Cite as Authors (Year) Title. American Mineralogist, in press.
DOI: https://doi.org/10.2138/am-2021-7473. http://www.minsocam.org/

**Table 1** A summary of EPMA chemical results of tourmaline from the Yushishanxi leucogranite.

| | Generation-I | | | Generation-II | | | Generation-III | | | Generation-IV | | |
|---|---|---|---|---|---|---|---|---|---|---|---|---|
| **Samples** | **Max** | **Min** | **Mean** | **Max** | **Min** | **Mean** | **Max** | **Min** | **Mean** | **Max** | **Min** | **Mean** |
| **$SiO_2$ (wt.%)** | 36.90 | 34.75 | 35.53 | 38.38 | 35.34 | 37.07 | 36.71 | 34.63 | 35.74 | 39.15 | 36.54 | 37.84 |
| **$TiO_2$** | 1.11 | 0.28 | 0.61 | 1.63 | 0.03 | 0.50 | 2.14 | 0.35 | 0.75 | 0.72 | 0.06 | 0.26 |
| **$Al_2O_3$** | 33.44 | 29.82 | 31.85 | 33.61 | 29.38 | 31.54 | 32.23 | 28.60 | 30.93 | 34.42 | 31.43 | 32.96 |
| **FeO** | 15.23 | 8.70 | 12.09 | 9.57 | 3.85 | 6.28 | 13.43 | 9.99 | 11.67 | 8.29 | 2.17 | 4.18 |
| **MnO** | 0.32 | 0.06 | 0.20 | 0.05 | 0.00 | 0.02 | 0.15 | 0.00 | 0.04 | 0.05 | 0.00 | 0.01 |
| **MgO** | 4.93 | 1.35 | 3.27 | 9.73 | 5.38 | 7.57 | 5.87 | 3.24 | 4.43 | 9.66 | 5.69 | 8.14 |
| **CaO** | 0.67 | 0.26 | 0.40 | 1.52 | 0.21 | 0.66 | 0.84 | 0.36 | 0.52 | 1.17 | 0.24 | 0.55 |
| **$Na_2O$** | 2.39 | 1.63 | 1.94 | 2.61 | 1.63 | 2.09 | 2.54 | 1.84 | 2.11 | 2.44 | 1.80 | 2.12 |
| **$K_2O$** | 0.08 | 0.03 | 0.05 | 0.06 | 0.01 | 0.03 | 0.06 | 0.01 | 0.04 | 0.05 | 0.00 | 0.03 |
| **F** | 1.10 | 0.13 | 0.46 | 0.60 | 0.00 | 0.20 | 0.54 | 0.00 | 0.11 | 0.56 | 0.00 | 0.10 |
| **$B_2O_3$*** | 10.50 | 10.09 | 10.28 | 10.78 | 10.35 | 10.57 | 10.48 | 10.19 | 10.33 | 10.92 | 10.44 | 10.72 |
| **$H_2O$*** | 3.51 | 3.02 | 3.33 | 3.71 | 3.35 | 3.56 | 3.62 | 3.35 | 3.51 | 3.75 | 3.44 | 3.65 |
| **F=O** | 0.46 | 0.05 | 0.19 | 0.25 | 0.00 | 0.08 | 0.23 | 0.00 | 0.05 | 0.23 | 0.00 | 0.04 |
| **total** | 101.15 | 98.51 | 99.82 | 101.79 | 98.23 | 100.00 | 101.48 | 98.37 | 100.13 | 101.59 | 99.16 | 100.51 |
| **Cations per formula unit normalized on the basis of 15(X+Y+Z) cations** | | | | | | | | | | | | |
| **B** | 3.00 | 3.00 | 3.00 | 3.00 | 3.00 | 3.00 | 3.00 | 3.00 | 3.00 | 3.00 | 3.00 | 3.00 |
| ***T-site*** | | | | | | | | | | | | |
| **Si** | 6.11 | 5.93 | 6.01 | 6.22 | 5.93 | 6.10 | 6.12 | 5.89 | 6.01 | 6.27 | 5.97 | 6.13 |
| **Al** | 0.07 | 0.00 | 0.01 | 0.07 | 0.00 | 0.00 | 0.11 | 0.00 | 0.03 | 0.03 | 0.00 | 0.00 |
| ***Z-site*** | | | | | | | | | | | | |
| **Al** | 6.00 | 6.00 | 6.00 | 6.00 | 5.77 | 5.97 | 6.00 | 5.68 | 5.99 | 6.00 | 6.00 | 6.00 |
| **Mg** | 0.00 | 0.00 | 0.00 | 0.11 | 0.00 | 0.01 | 0.27 | 0.00 | 0.01 | 0.00 | 0.00 | 0.00 |
| ***Y-site*** | | | | | | | | | | | | |
| **Al** | 0.57 | 0.04 | 0.34 | 0.43 | 0.00 | 0.14 | 0.37 | 0.00 | 0.11 | 0.50 | 0.07 | 0.30 |
| **Ti** | 0.14 | 0.04 | 0.08 | 0.20 | 0.00 | 0.06 | 0.27 | 0.04 | 0.09 | 0.09 | 0.01 | 0.03 |
| **Fe** | 2.16 | 1.20 | 1.71 | 1.34 | 0.54 | 0.87 | 1.88 | 1.39 | 1.64 | 1.15 | 0.29 | 0.57 |
| **Mg** | 1.22 | 0.34 | 0.82 | 2.29 | 1.31 | 1.85 | 1.34 | 0.81 | 1.10 | 2.29 | 1.41 | 1.96 |
| **Mn** | 0.05 | 0.01 | 0.03 | 0.01 | 0.00 | 0.00 | 0.02 | 0.00 | 0.01 | 0.01 | 0.00 | 0.00 |
| **ΣY** | 3.00 | 2.89 | 2.98 | 3.00 | 2.78 | 2.92 | 3.00 | 2.88 | 2.96 | 3.00 | 2.73 | 2.86 |
| **Al total** | 6.57 | 6.04 | 6.34 | 6.43 | 5.77 | 6.11 | 6.37 | 5.68 | 6.10 | 6.50 | 6.07 | 6.30 |
| ***X-site*** | | | | | | | | | | | | |
| **Ca** | 0.12 | 0.05 | 0.07 | 0.27 | 0.04 | 0.12 | 0.15 | 0.07 | 0.09 | 0.20 | 0.04 | 0.10 |
| **Na** | 0.78 | 0.53 | 0.64 | 0.85 | 0.51 | 0.67 | 0.83 | 0.60 | 0.69 | 0.76 | 0.57 | 0.67 |
| **K** | 0.02 | 0.01 | 0.01 | 0.01 | 0.00 | 0.01 | 0.01 | 0.00 | 0.01 | 0.01 | 0.00 | 0.01 |
| **Xvac** | 0.39 | 0.10 | 0.28 | 0.35 | 0.01 | 0.21 | 0.31 | 0.06 | 0.21 | 0.39 | 0.14 | 0.23 |
| ***V+W-site*** | | | | | | | | | | | | |
| **F** | 0.59 | 0.07 | 0.25 | 0.31 | 0.00 | 0.10 | 0.28 | 0.00 | 0.06 | 0.28 | 0.00 | 0.05 |
| **OH** | 3.93 | 3.41 | 3.75 | 4.00 | 3.69 | 3.90 | 4.00 | 3.72 | 3.94 | 4.00 | 3.72 | 3.95 |

Note: The structural formulae are calculated on the basis of 15 cations in the tetrahedral and octahedral sites (T+Z+Y) of the tourmaline. $B_2O_3$* and $H_2O$ are calculated on stoichiometry for B = 3 apfu and OH+F = 4 apfu.

Figure 1

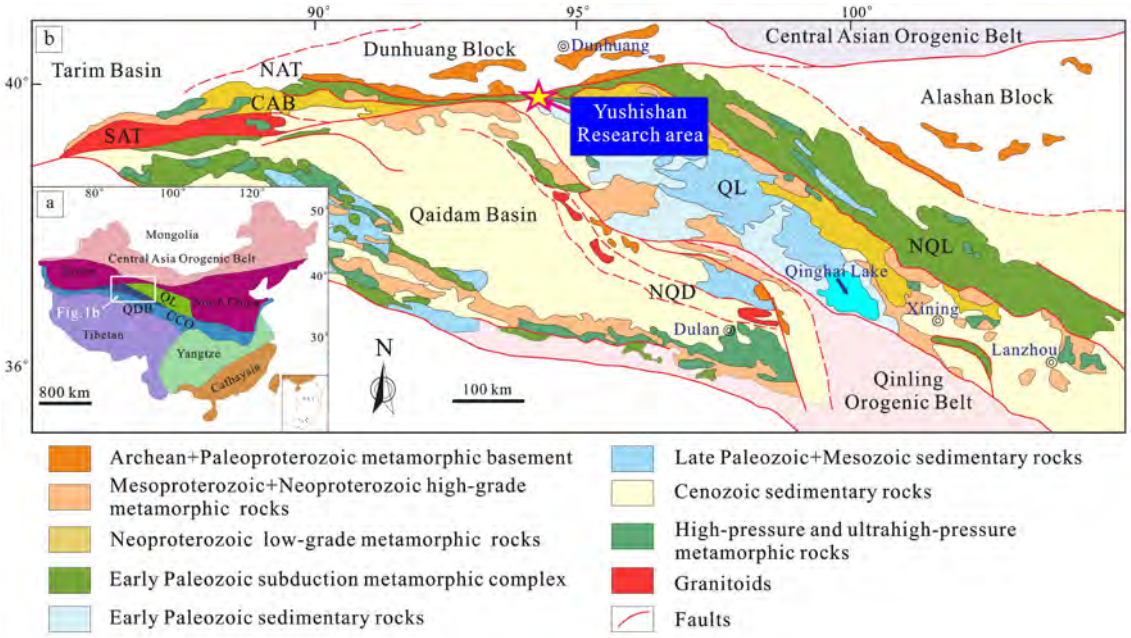

Figure 2

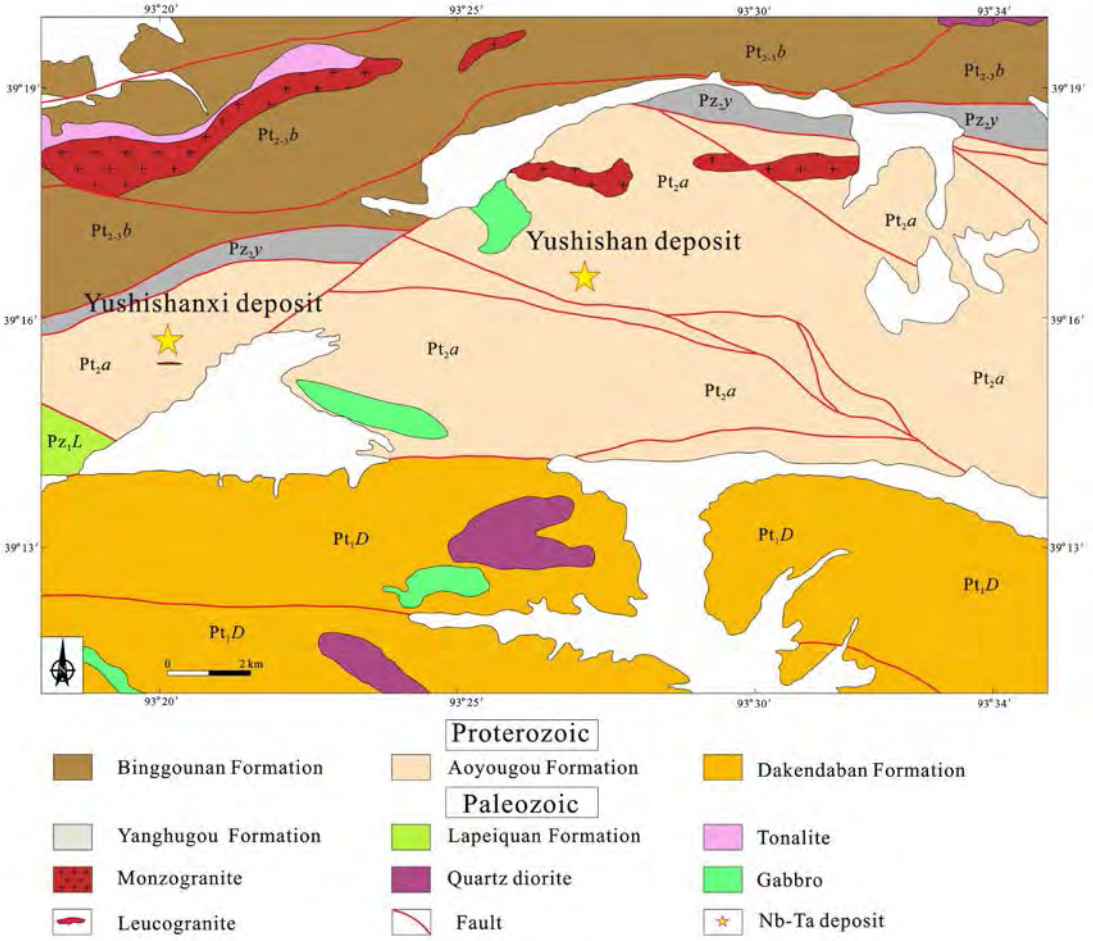

Figure 3

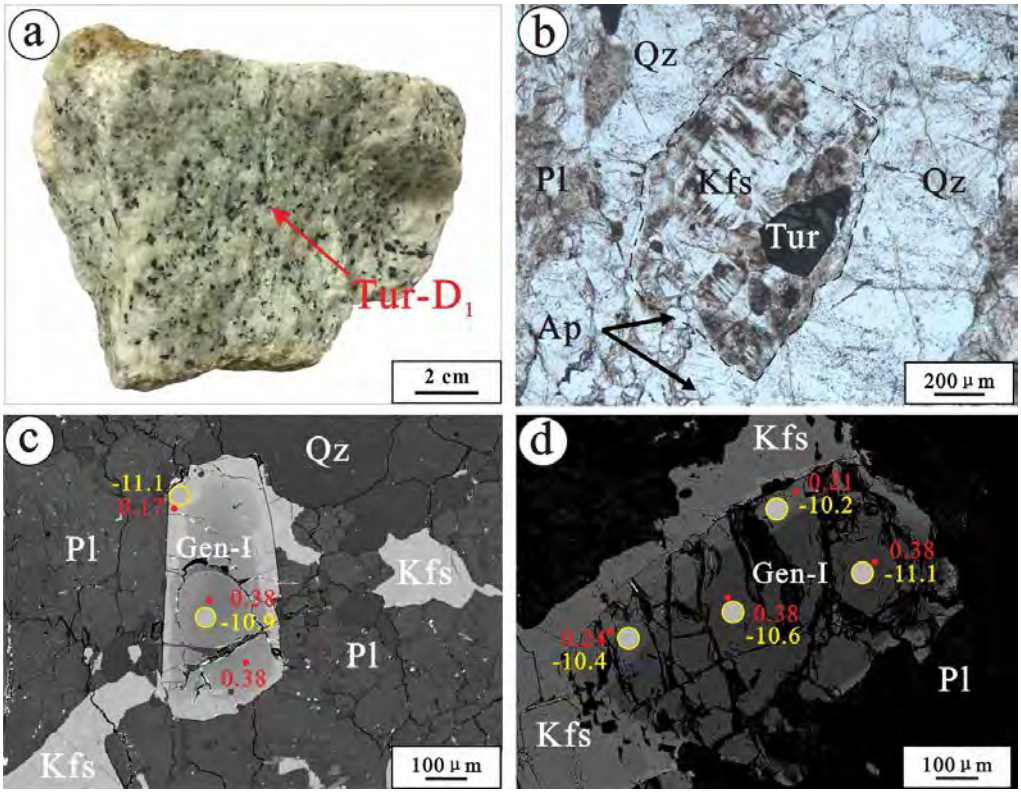

Figure 4

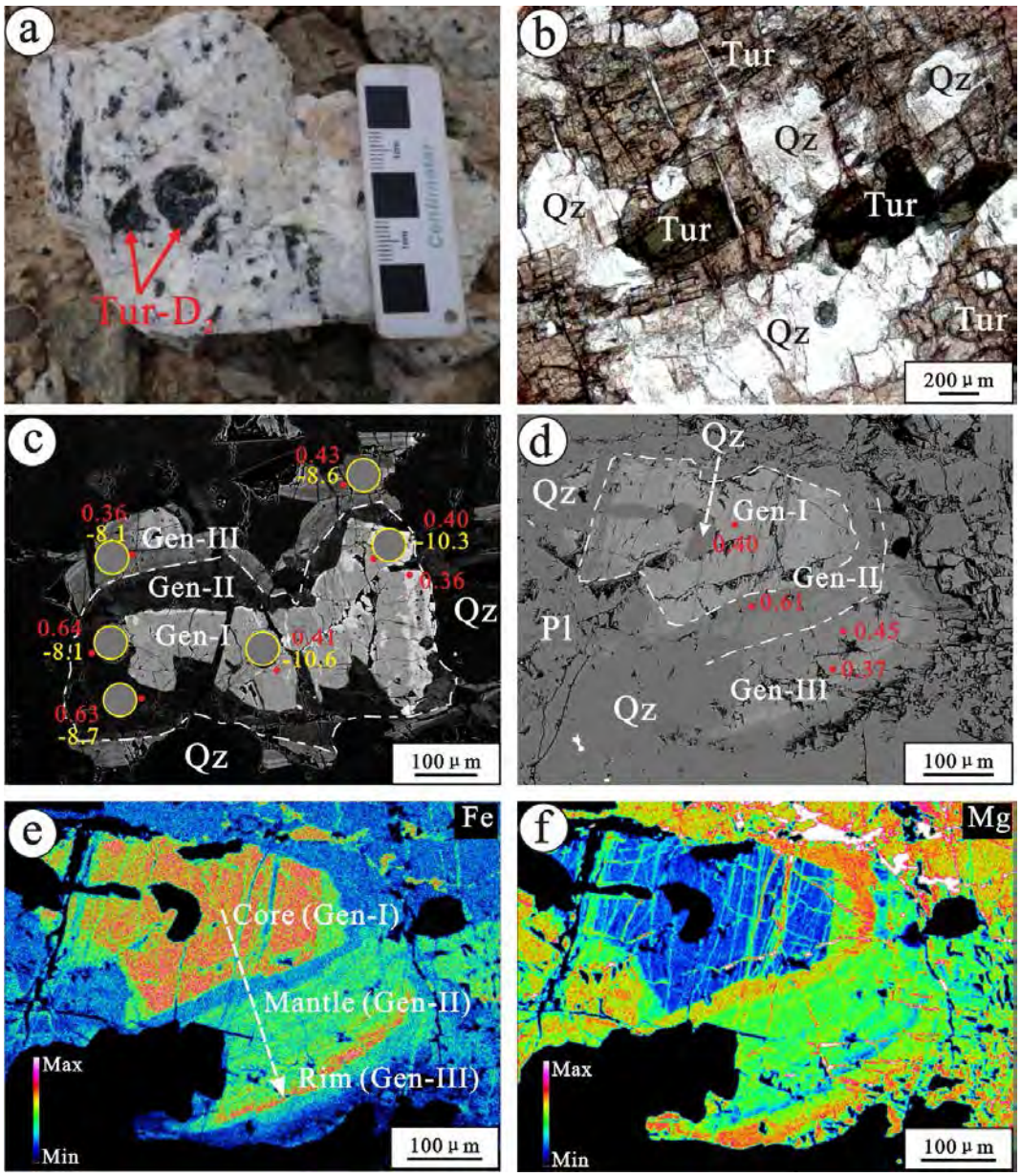

Figure 5

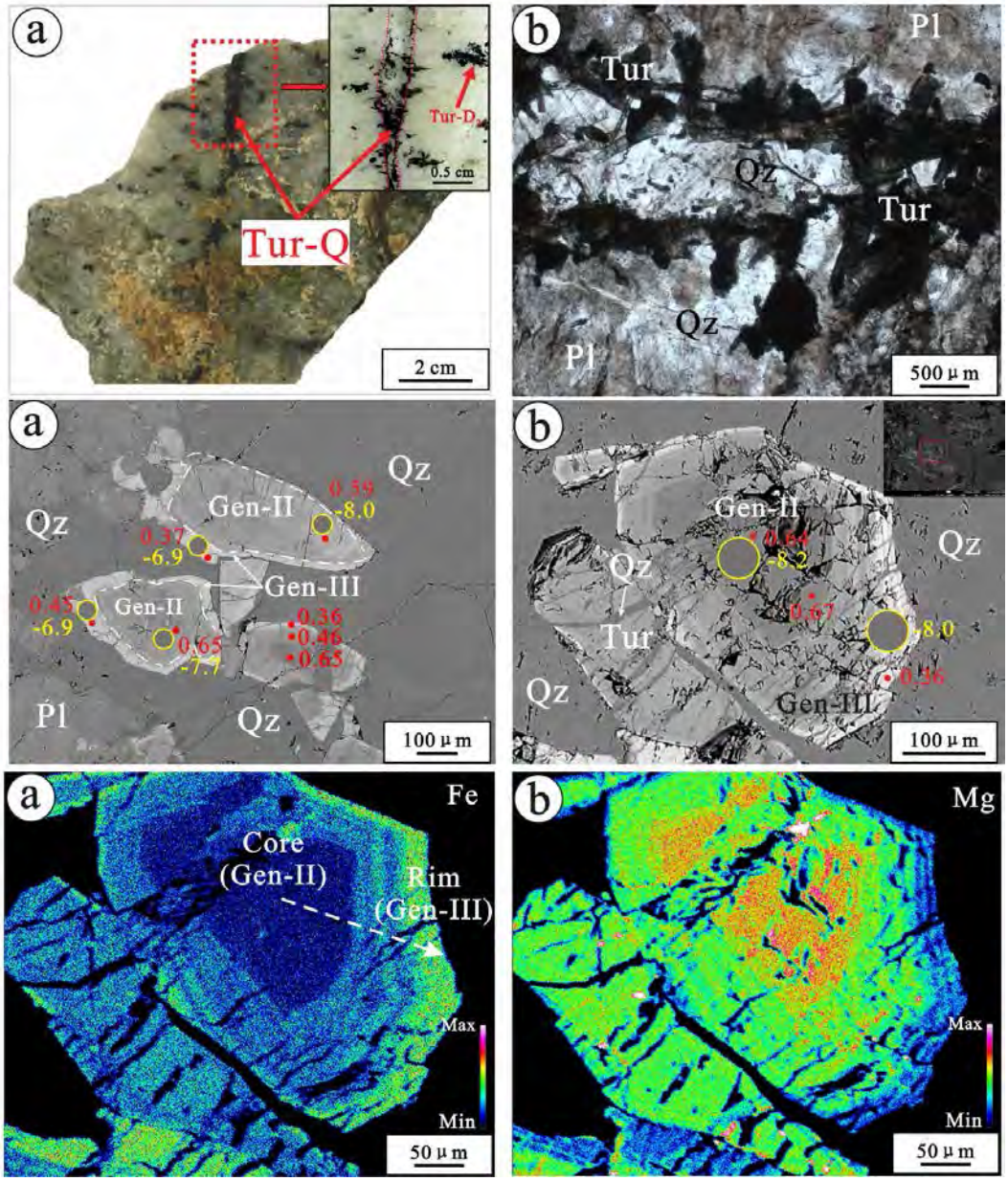

This is the peer-reviewed, final accepted version for American Mineralogist, published by the Mineralogical Society of America.
The published version is subject to change. Cite as Authors (Year) Title. American Mineralogist, in press.
DOI: https://doi.org/10.2138/am-2021-7473. http://www.minsocam.org/

Figure 6

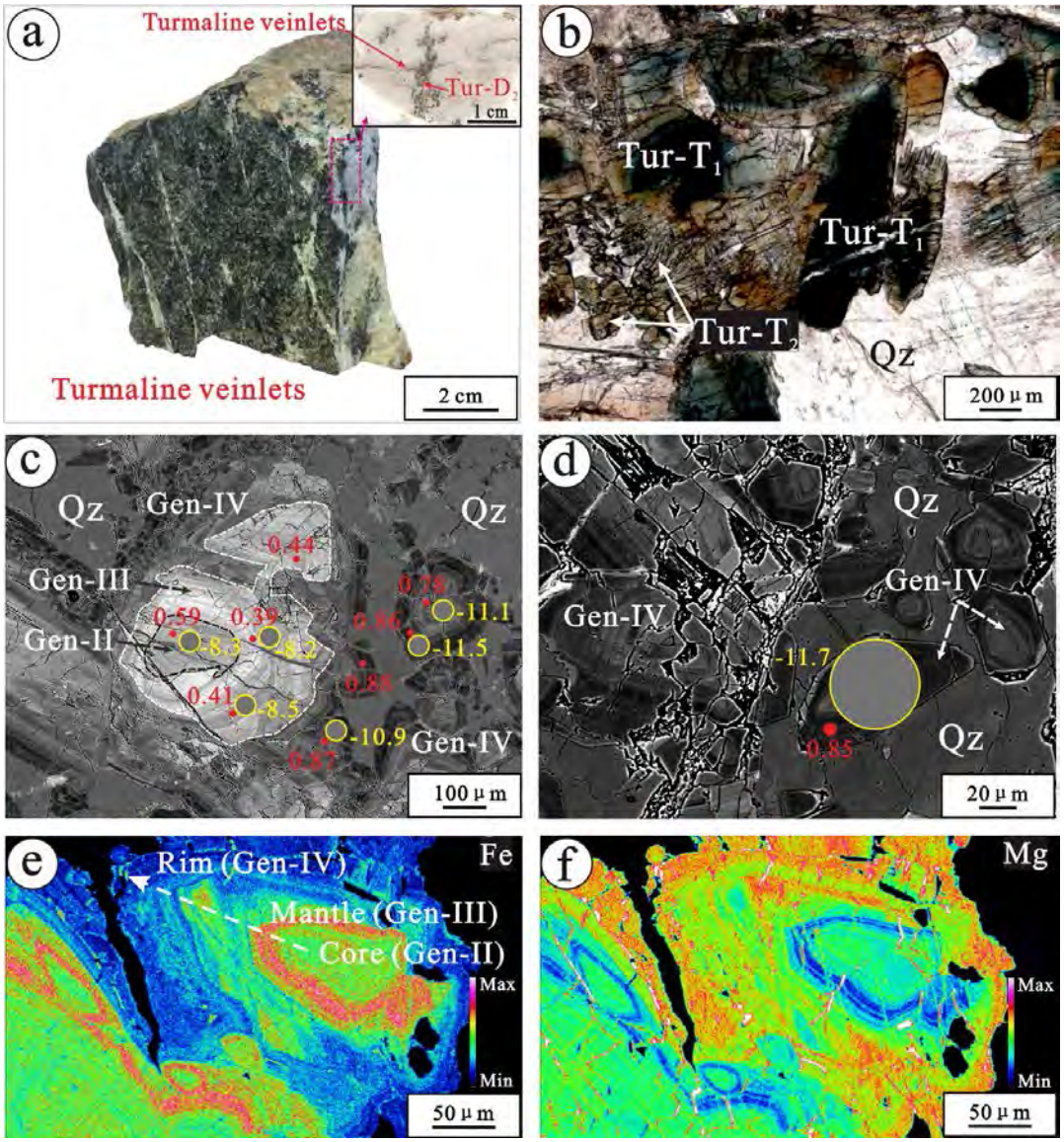

This is the peer-reviewed, final accepted version for American Mineralogist, published by the Mineralogical Society of America.
The published version is subject to change. Cite as Authors (Year) Title. American Mineralogist, in press.
DOI: https://doi.org/10.2138/am-2021-7473. http://www.minsocam.org/

Figure 7

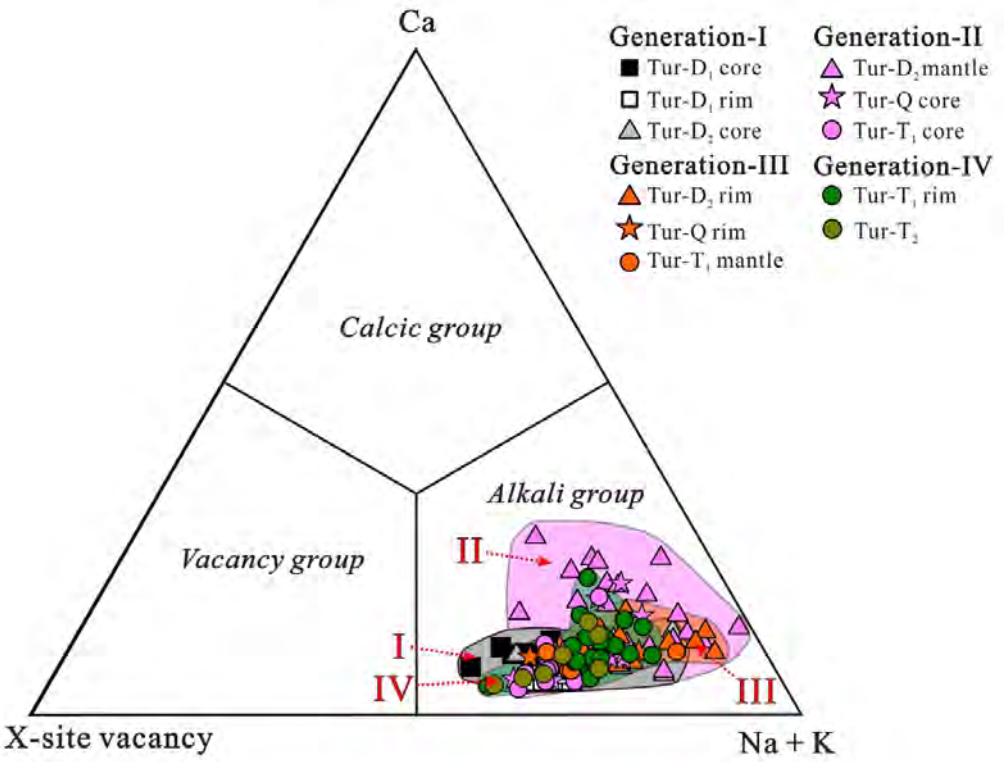

Figure 8

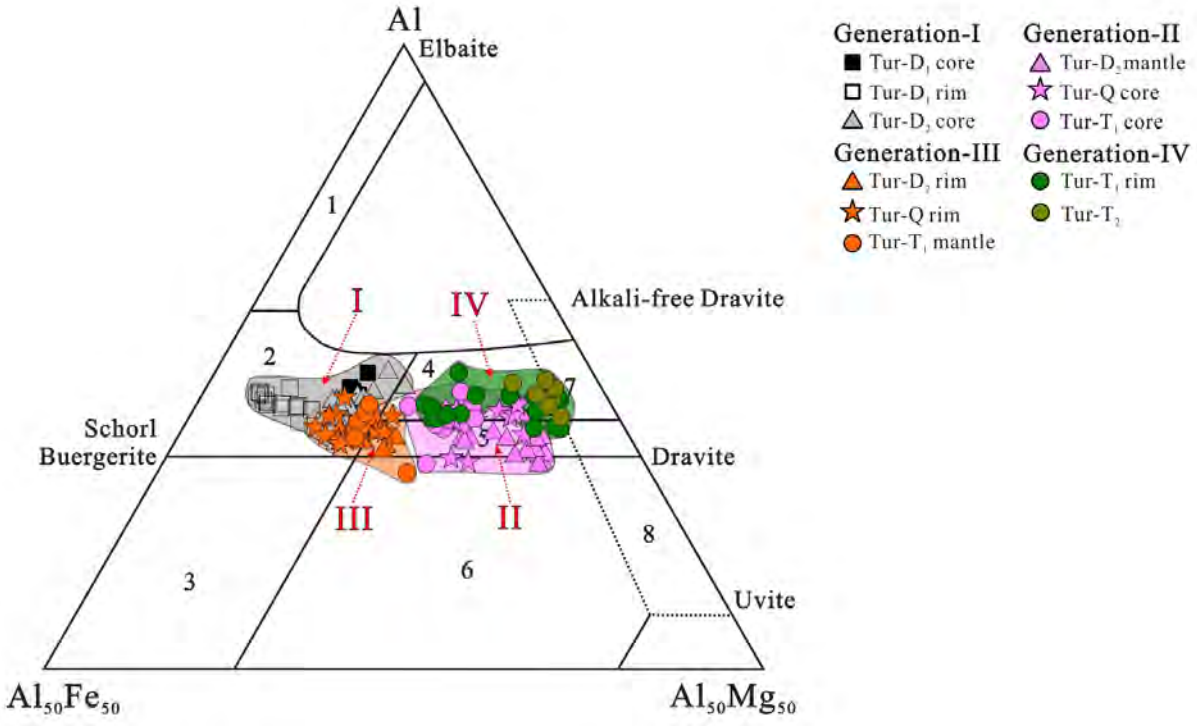

Figure 9

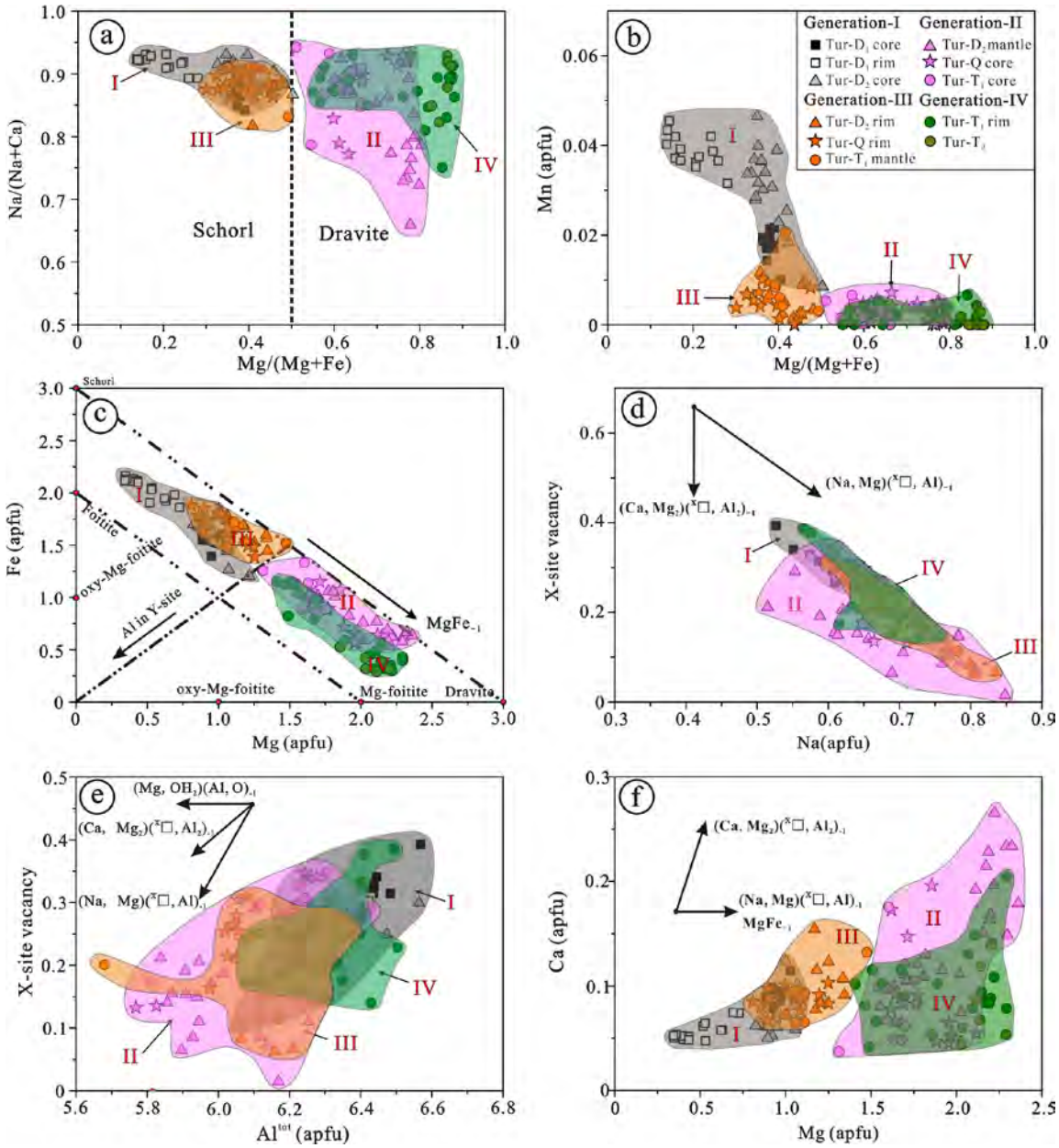

Figure 10

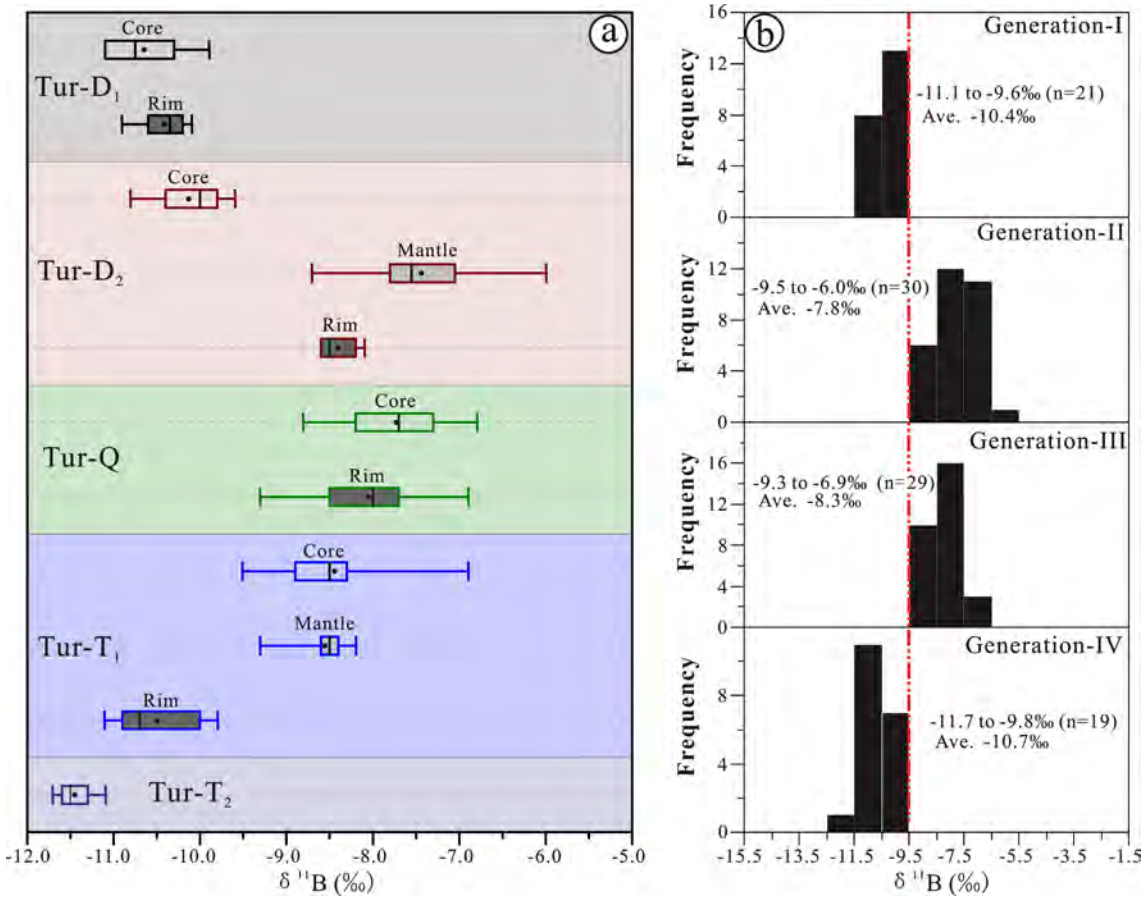

This is the peer-reviewed, final accepted version for American Mineralogist, published by the Mineralogical Society of America.
The published version is subject to change. Cite as Authors (Year) Title. American Mineralogist, in press.
DOI: https://doi.org/10.2138/am-2021-7473. http://www.minsocam.org/

Figure 11

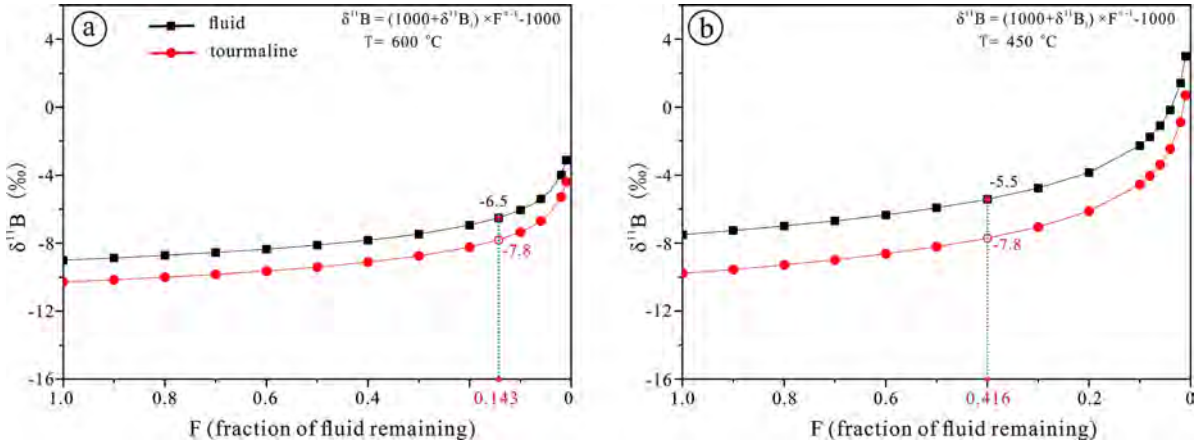

Figure 12